Available online at www.sciencedirect.com
ScienceDirect
Acta Materialia 58 (2010) 4387–4397
Acta MATERIALIA
www.elsevier.com/locate/actamat

Solid-state foaming of Ti–6Al–4V by creep or superplastic expansion of argon-filled pores

Scott Oppenheimer [1], David C. Dunand *

Department of Materials Science and Engineering, Northwestern University, Evanston, IL 60208, USA

Received 2 March 2010; received in revised form 20 April 2010; accepted 21 April 2010
Available online 28 May 2010

Abstract

Ti–6Al–4V foams are produced by the expansion of pressurized argon pores trapped in billets created by powder metallurgy. Pore expansion during thermal cycling (840–1030 °C, which induces transformation superplasticity in Ti–6Al–4V) improves both the foaming rate (by reducing the flow stress) and the final porosity (by delaying fracture of the pores and subsequent escape of the gas), as compared to isothermal pore expansion at 1030 °C, where Ti–6Al–4V creep is the controlling mechanism. Raising the argon content in the billet increases the foaming rates for both creep and superplastic conditions, in general agreement with an analytical model taking into account the non-ideal behavior of high-pressure Ar and the pore size dependence of surface tension. Superplastically foamed Ti–6Al–4V with 52% open porosity exhibits a combination of high strength (170 MPa) and low stiffness (18 GPa), which is useful for bone implant applications.

Keywords: Cellular materials; Porous materials; Titanium; Creep; Superplasticity

1. Introduction

Porous titanium and titanium alloys are attractive for biomedical implants, catalyst substrates, and aerospace sandwiches [1–3]. With titanium, liquid-based metal foaming methods (e.g. gas injection or addition of foaming agents to a melt, and replication casting) used for aluminum and other metals [4,5] are very challenging, because titanium exhibits a high melting point, strong reactivity with most solid materials and high tendency for contamination by trace atmospheric gases (in particular oxygen, which leads to rapid embrittlement). Therefore, titanium foams are mostly produced by powder-metallurgy methods, as reviewed in Ref. [3]: (i) partial sintering of powders [6–8], hollow spheres [9] or mixtures of powders and temporary space-holders [10–14]; or (ii) localized sintering or melting of powders via rapid prototyping methods [15–17].

An alternative method, based on expansion of pressurized pores trapped within a solid alloy compacted from powders, was first demonstrated by Kearns et al. [18] for Ti–6Al–4V. In a first step, Ti–6Al–4V powders are compacted in the presence of argon gas by hot isostatic pressing, resulting in a dense billet containing a small fraction of isolated, high-pressure, micron-size pores. These argon-filled pores are then expanded through creep of the surrounding alloy during a high-temperature annealing step. This method has also been used to create high levels of porosity in commercially pure titanium (CP-Ti) [19,20] and the near-equiatomic Ni–Ti alloy (Nitinol) [21,22]. Significant increases in foaming rates are achieved in CP-Ti when cycling about the allotropic transformation temperature during the argon expansion annealing step. This induces transformation superplasticity [19,23–25], which reduces the creep strength of CP-Ti and thus its resistance to the expansion of the argon-filled pores, as compared to

* Corresponding author. Tel.: +1 847 491 5370.
E-mail address: dunand@northwestern.edu (D.C. Dunand).
[1] Present address: ATI Allvac, 2020 Ashcraft Ave, Monroe, NC 28111-5030, USA.

1359-6454/$36.00 © 2010 Acta Materialia Inc. Published by Elsevier Ltd. All rights reserved.
doi:10.1016/j.actamat.2010.04.034

isothermal foaming, where creep is the dominant deformation mechanism. Also, transformation superplasticity increases ductility [26,27], thus delaying fracture of the pore walls and gas escape, thus increasing the terminal porosity of the foams.

While transformation superplasticity has been studied in bulk Ti–6Al–4V [26,28–32], it has never been used to foam this alloy by gas expansion. The goal of the present study is to demonstrate superplastic foaming of Ti–6Al–4V and study the effect of the main processing parameters: argon backfill pressure, initial pore size and cycling period. The superplastic foaming kinetics are compared to those for isothermal foaming, and also modeled numerically and analytically. Finally, the mechanical properties of the Ti–6Al–4V foams are measured.

2. Experimental methods

2.1. Densification and foaming

Spherical Ti–6Al–4V powders (Grade 5, from Starmet Corp., Concord, MA) were sieved to three different average sizes: 75 μm (62–88 μm, −170/+230 mesh), 115 μm (105–125 μm, −120/+140 mesh) and 165 μm (149–177 μm, −80/+100 mesh). One mild steel canister (50.8 mm outer diameter) was filled with individual layers of the three above powders, labeled A, B and C, respectively. After evacuation and backfill with 0.33 MPa argon gas, the canister was welded shut and densified by hot isostatic pressing (HIP) at 950 °C at 100 MPa pressure for 4 h. Four steel tubes (9.53 mm outer diameter and 7.04 mm inside diameter) were filled with 115 μm powders and backfilled with 0.1–0.32 MPa Ar (calculated from the amount of metered argon). These welded tubes were then HIP densified at 980 °C under 100 MPa argon for 4 h and are labeled B1–B4. Table 1 summarizes the experimental conditions for the seven specimens. Cubic specimens with 9 mm edges were electrodischarge machined from the large densified billets A–C. The steel layer of the smaller billets (B1–4) was removed electrochemically by immersion in a 10% acetic acid solution with an applied voltage of 1.5 V-dc, polished with 600 grit sandpaper and cut into cylindrical sections 20–30 mm in length and ~6 mm in diameter.

Table 1
Experimental conditions for billets.

Samples	Powder average size (μm)	Argon backfill pressure (MPa)	Initial porosity f_0 (%)	HIP temperature (°C)
A	75	0.33	0.35	950
B[a]	115	0.33	0.36	
C	165	0.33	0.32	
B1	115	0.32[c]	0.48	980
B2	115	0.1[b,c]	0.09	
B3	115	0.17[c]	0.24	
B4	115	0.28[c]	0.36	

[a] Only used for cycling rate studies.
[b] Low accuracy due to some gas loss during can welding.
[c] Calculated from metering of gas, not from pressure gage.

Foaming was preformed in a vacuum furnace (with a maximum residual pressure during initial heat up of 2×10^{-5} Torr dropping by a factor of ten at equilibrium). All the isothermal foaming experiments were performed at 1030 °C, with a 25.4 mm outer diameter, 100 mm high titanium tube placed around the sample to act as a getter. The temperature was measured by a K-type thermocouple coated with boron nitride at the titanium getter tube (previous calibration tests had shown no measurable temperature gradient between the tube and the sample). Foaming under thermal cycling condition was carried out between 840 and 990 °C for the cycling rate experiments or between 840 and 1030 °C for all other experiments. For the former experiments 2, 4 and 8 min cycles were used, while the latter experiments were carried out with 8 min cycles. In all cases the temperature was measured by a type K thermocouple coated in boron nitride in direct contact with the sample.

2.2. Density measurements

The foaming experiments were periodically interrupted to measure the foam closed porosity by helium pycnometry and the foam density ρ_{foam} by the Archimedes method using:

$$\rho_{foam} = \frac{m_{air} - m_{water}}{\rho_{water}} \quad (1)$$

where m_{air} and m_{water} are the mass of the foam in air and in water, and ρ_{water} is the temperature-dependent density of water. The total porosity P was then calculated as:

$$P = \frac{\rho_{metal} - \rho_{foam}}{\rho_{metal} - \rho_{Ar}} \quad (2)$$

where ρ_{metal} is the density of Ti–6Al–4V and ρ_{Ar} is the density of Ar calculated by the Virial equation with coefficients taken from Ref. [33]. The immersed sample mass m_{water} has ±0.3 mg error due to surface tension, air pressure variations and the scale error (0.1 mg). With standard error propagation, the porosity of a 1 cm^3 sample has an absolute error of ±0.03%, which is significant when compared to the smallest measured initial billet porosity (0.09%). Since each sample was measured at least 10 times, the 95% confidence interval of the average initial porosity, listed in Table 1, is about ±0.01%.

A systematic source of error is associated with the precise determination of ρ_{metal}, which depends on the exact level of the alloying elements Al and V. In previous studies on commercially pure Ti and NiTi [21,24], the density of the bulk material was measured from a sample arc melted from the powders used for foaming to eliminate density errors associated with variation in alloy composition. This method is less accurate in Ti–6Al–4V due to the dual phase nature of Ti–6Al–4V at room temperature consisting of a denser cubic β-phase and a less dense hexagonal α-phase.

As both compositions and volume fractions of these phases are dependent on the thermal history, the density of a control Ti–6Al–4V sample produced by arc melting and rapid cooling is not the same as that of the slow-cooled HIPed Ti–6Al–4V samples.

To determine the exact density ρ_{metal} of the Ti–6Al–4V used in the foam, the following steps were taken. First, a section of as-HIP Ti–6Al–4V was vacuum arc melted into a 5.69 g sample whose density in the as-solidified state was measured by the Archimedes method (30 measurements) as 4.4292 ± 0.0005 g cm^{-3}. Next, the α-phase fraction was determined through SEM backscatter image analysis as 84.9% and 91.5% for the as-HIP B1 billet and the arc-melted B sample, respectively. Then, to relate the phase fraction to the density, the thermodynamic software JMat Pro (Sente Software Ltd.) was used to estimate the density of Ti–6Al–4V heat-treated to create the above α-Ti phase fractions. The results are 4.50126 g cm^{-3} for 91.5% α-phase (corresponding to the arc melted sample) and 4.49903 g cm^{-3} for 84.9% α-phase (corresponding to the matrix of the HIP sample). While the absolute densities are different for the calculated and measured arc-melted samples (possibly because many Al/V ratios can give the same α-Ti fraction), the ratio of the above densities ($R = 4.49903/4.50126$) can be used to estimate the density of the matrix of the HIP sample as $R * 4.4292 = 4.4270$ g cm^{-3}.

2.3. Microstructure and mechanical properties measurements

For metallographic examination, samples were sectioned, mounted in phenolic resin and polished to 0.05 μm alumina. Pore size distributions were determined by digital image analysis from scanning electron microscope (SEM) micrographs. The images were processed to create a binary black and white image, which was then analyzed by the software ImageJ. The pore areas were determined and the effective two-dimensional diameter calculated (assuming circular shape). These diameters were then distributed into fifteen bins. Using Saltykov analysis [34,35], the two-dimensional size of bin i was calculated as $D_{\max}10^{-0.1(i-1)}$, where $D_{\max}$ is the largest pore diameter (corresponding to the largest pore). For each bin size, a calculation [34,35] was run to find the corresponding three-dimensional pore diameter distributions. Due to the iterative nature of this method, a few pores with negative sizes were found, and these were discarded as artifacts.

Compressive mechanical properties were measured on samples with 6 mm diameter and 12 mm height, using a compression cage in a screw-driven universal testing machine, with strain calculated from cross-head displacement after correction for the machine compliance determined prior to the test. The Young's modulus was calculated using standard equations [21] from sound velocity values measured ultrasonically in transmission using two transducers operating at 5 MHz.

3. Results

3.1. Foaming kinetics

As expected, the initial porosity scales linearly, within experimental error, with the Ar backfill pressure (Table 1) for samples B1–B4 densified at the same temperature, and the initial porosity is constant for samples A–C, within experimental error, which were backfilled with the same Ar pressure.

Fig. 1a shows the evolution of porosity during isothermal annealing at 1030 °C of foams A, C and B1–B4 with initial porosities $f_0 = 0.09$–0.48%. As reported previously for CP-Ti [19,25,36–38], the foaming rate decreases monotonically with time, as expected from the decrease in gas pressure associated with the increase in pore volume. For a given foaming time, the rate of porosity growth (slope of the curve in Fig. 1a) increases with increasing initial porosity, as expected from the increase in initial argon

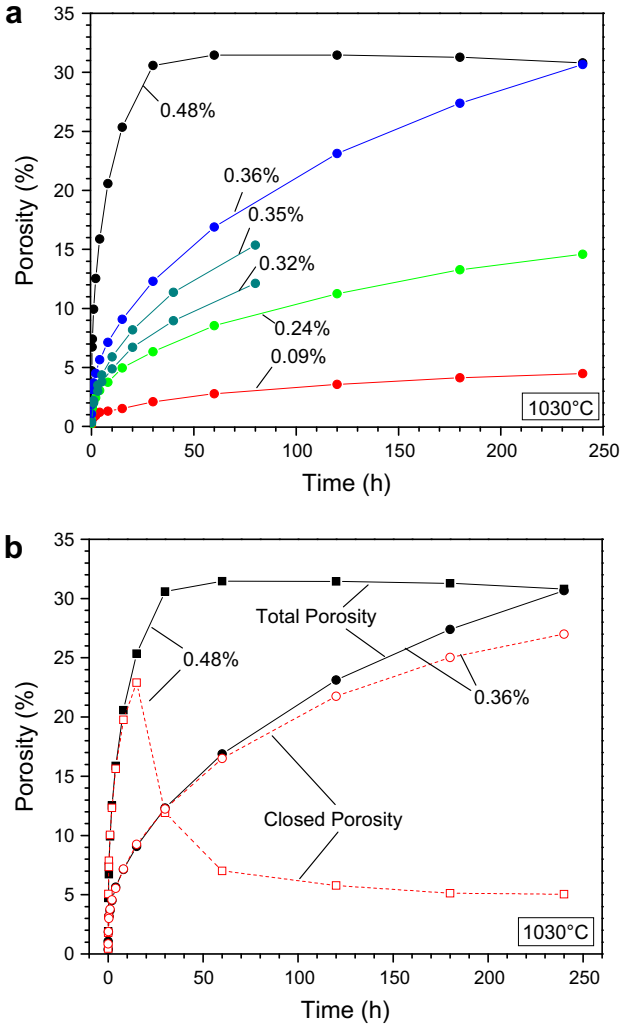

Fig. 1. Isothermal foaming curves showing (a) total porosity vs. time for samples with various initial porosities and (b) total porosity and closed porosity vs. time for samples A, C and B1–B4.

content. In Fig. 1b, the total and closed porosity are shown for the two foams with the highest initial porosity ($f_0 = 0.36\%$ and 0.48%). For sample B4 ($f_0 = 0.36\%$), porosity starts to open when total porosity reaches a value of ~22%. This is also true for foam B1 ($f_0 = 0.48\%$), with a first measurable open porosity for a total porosity of ~24%, followed by rapid opening of the porosity associated with an abrupt cessation of foaming. The other four foams shown in Fig. 1a, with lower initial porosities and final porosities below 15%, show no measurable open porosity for the annealing times used here.

Fig. 2a shows the porosity evolution under thermal cycling conditions (840–990 °C) for three specimens of foam B ($f_0 = 0.36\%$) cycled with 2, 4 and 8 min periods. As compared to isothermal conditions, foaming is much more rapid, and the maximum porosity achieved (46%) exceeds all those shown in Fig. 1a, even for billets with higher initial porosity. The curves are near linear, indicating that additional foaming may be achievable with further thermal cycling. Decreasing the cycling period leads to only a small gain in foaming rate. As shown in Fig. 2b, where porosity is plotted as a function of cycle number, this is because faster thermal cycle rates (i.e. shorter cycling periods) lead to lower porosity growth rate per cycle.

Fig. 3 shows the foaming behavior of samples B1–B4 with different initial porosities ($f_0 = 0.09$–0.48%) for thermal cycling between 840 and 1030 °C with 8 min cycles. As in Fig. 2a (for $f_0 = 0.36\%$), the porosity increases at first linearly with time, with the initial foaming rate scaling linearly with the initial porosity. After reaching a value of ~40%, porosity abruptly stops growing, as the pores open the surface and release the entrapped Ar. In fact, the porosity decreases noticeably with further cycling for the two foams with the highest initial porosities ($f_0 = 0.36$–0.48%).

3.2. Foam microstructure

Figs. 4 and 5 show metallographic cross-sections of foam B1 ($f_0 = 0.48\%$) after various foaming times under isothermal (Fig. 4a–d) and cycling conditions (Fig. 5a–d). Since metallographic preparation is destructive, each micrograph represents a different sample from the same billet. Under isothermal conditions at 1030 °C, pores grow rapidly to 9% porosity after 1 h of foaming (Fig. 4b), then much more slowly to 21% porosity after 8 h (Fig. 4c) and to 29% porosity after 60 h (Fig. 4d). The pores are initially equiaxed and isolated in the cross-sections (Fig. 4b), but then connect to each other, forming a continuous path (Fig. 4c and d). As shown in Fig. 1b, the foam corresponding to Fig. 4d has mostly open porosity.

After ~1 h of thermal cycling (840–1030 °C), the pore size and fraction (Fig. 5b) is quite similar to that achieved isothermally (Fig. 4b), despite the lower average temperature during cycling. Upon further cycling for 3.5 h, a porosity of 24% is reached (Fig. 5c), as compared to 21% porosity after 8 h during isothermal foaming (Fig. 4c). In both cases, pores appear mostly unconnected to each other

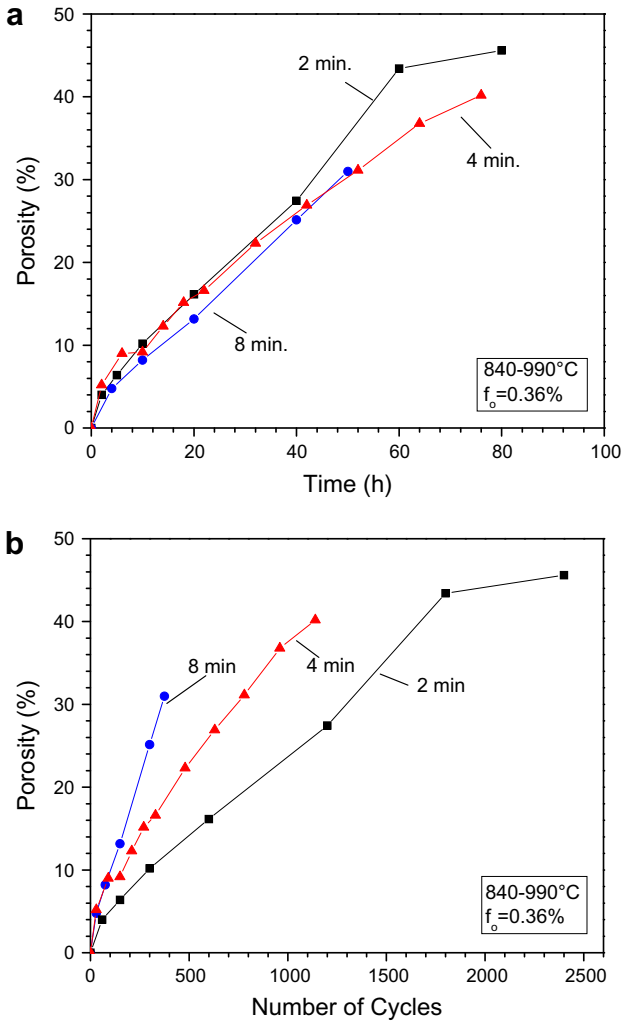

Fig. 2. Total porosity for sample B cycled at 840–990 °C with various cycling periods plotted as functions of (a) time and (b) number of cycles.

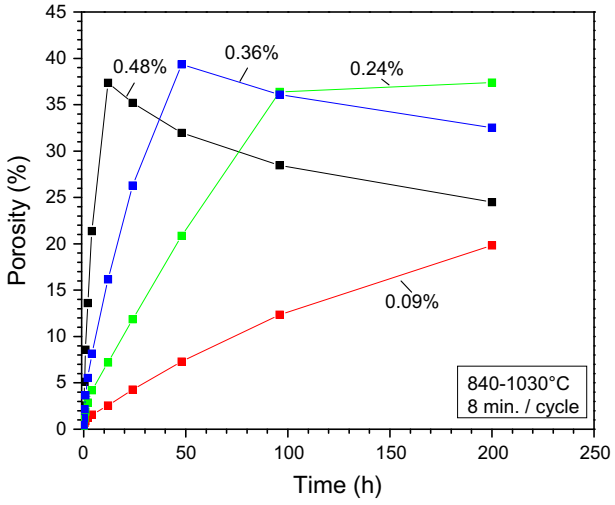

Fig. 3. Foaming curves for 840–1030 °C cycling showing total porosity vs. time for samples B1–B4 with different initial porosities.

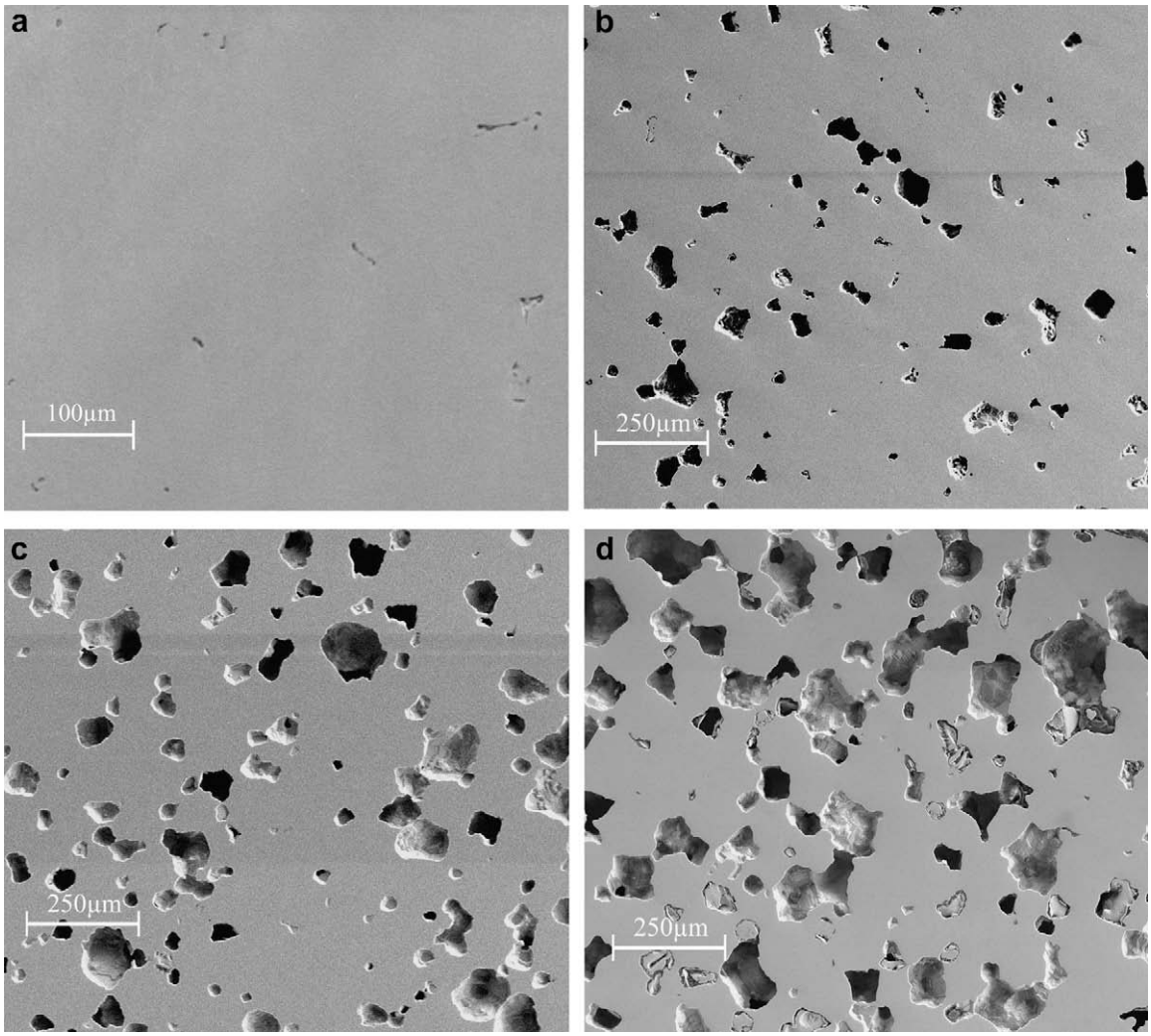

Fig. 4. SEM micrographs of polished cross-sections for isothermally annealed samples B1: (a) with 0.48% initial porosity samples in the as-HIP state; (b) with 9% porosity after 60 min of isothermal annealing; (c) with 21% porosity after 8 h of isothermal annealing; (d) with 29% porosity after 60 h of isothermal annealing.

in the cross-sections. Finally, Fig. 5d shows a high porosity of 41% porosity achieved after 10 h of cycling. Pores have merged with each other, but their shape is more rounded than those shown in Fig. 4d for isothermal foaming (29% porosity after 60 h), indicating a higher level of matrix deformation, as expected from the higher porosity.

In micrographs of both isothermal and cycled foams, many pores show blocky shapes, as also reported for isothermally foamed Ti–6Al–4V by Kearns et al. [18], who assign this phenomenon to the anisotropic surface energy of Ti–6Al–4V. Direct comparison is difficult because the current study was carried out at lower temperatures, and the thermal cycling may allow for changes in the grain crystallographic orientations, which might enhance or reduce this effect.

Fig. 6 shows the pore radius distribution, as calculated using the Saltykov analysis on cross-sections of four foamed samples with 9–20% porosity produced under isothermal or thermal cycling conditions. While the small pores (10–20 μm) dominate by numbers, the largest size pores affect disproportionately the total porosity, which scales with pore volume. Two peaks appear in the distributions, the second peak, at the larger size, probably corresponding to clusters of merged pores.

3.3. Foam mechanical properties

Fig. 7 shows compressive stress–strain curves for foams produced by both methods (isothermal and cyclic foaming) and with various porosities (9–52%). All curves show similar features: an elastic region, a plateau region associated with pore collapse, and a densification region at the onset of which the test was terminated. As porosity increases, the yield and plateau stress decrease, while the strain in the plateau region before onset of densification increases. The energy absorbed to 30% compression ranges between 70 J g^{-1} (250 J cm^{-3}) for the foam with 21% porosity and 36 J g^{-1} (75 J cm^{-3}) for the foam with 52% porosity.

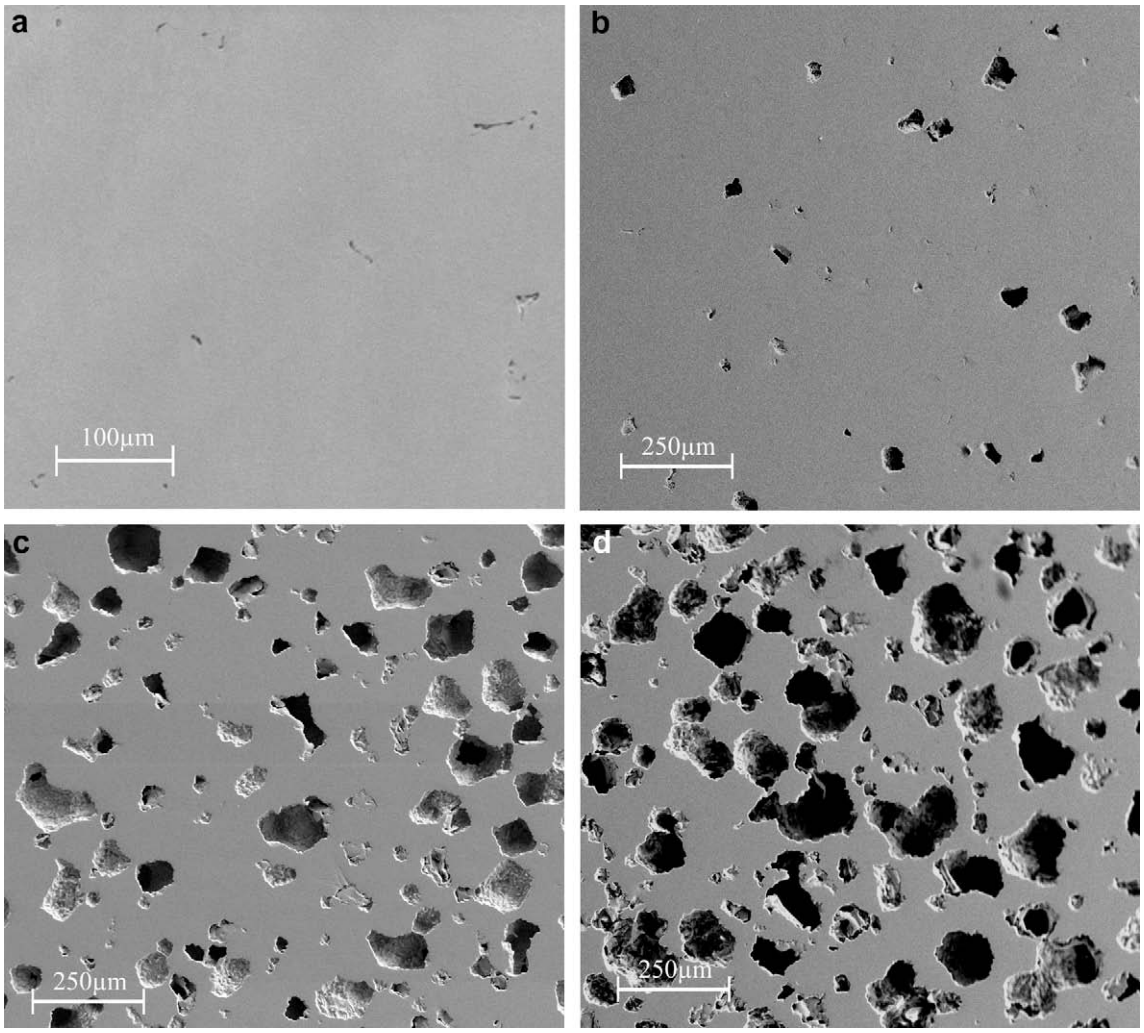

Fig. 5. SEM micrographs of polished cross-sections for samples B1 thermally cycled at 840–1030 °C (a) with 0.48% initial porosity samples in the as-HIP state; (b) with 8% porosity after 56 min of cycling; (c) with 24% porosity after 3.5 h of cycling; (d) with 41% porosity after 10 h of cycling.

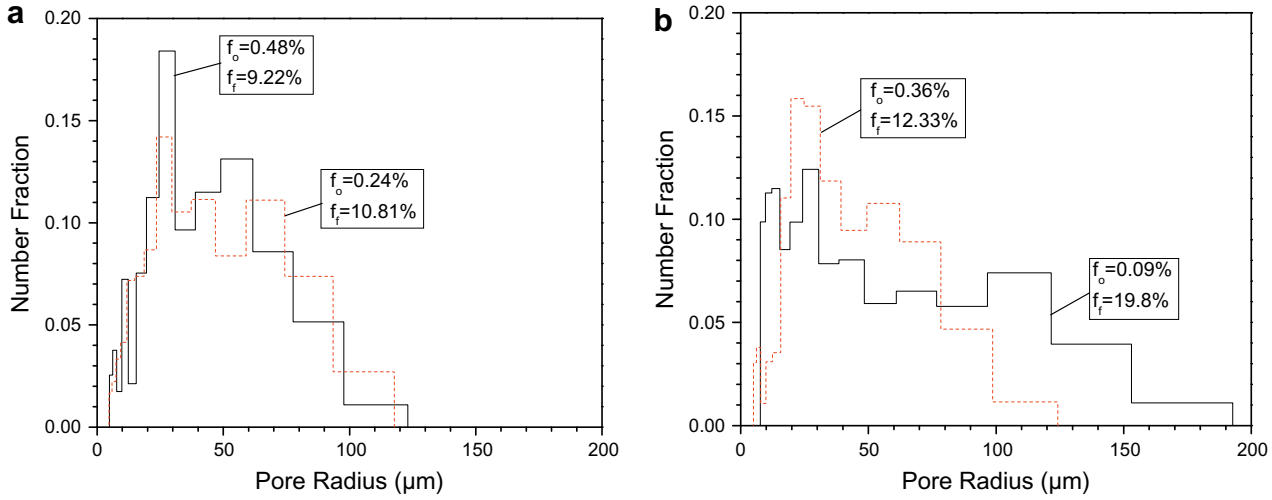

Fig. 6. Pore size distributions as determined from cross-sections: (a) B1 with 9.2% porosity after 64 min of isothermal annealing; (b) B2 with 19.8% porosity after 200 h of 840–1030 °C cycling; (c) B3 with 10.8% porosity after 24 h of 840–1030 °C cycling (d) B4 with 12.3% porosity after 8 h of 840–1030 °C cycling.

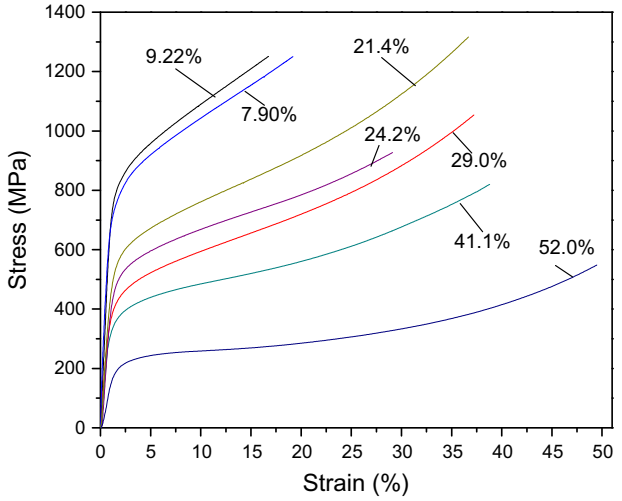

Fig. 7. Compressive stress–strain curves for foams with various porosities.

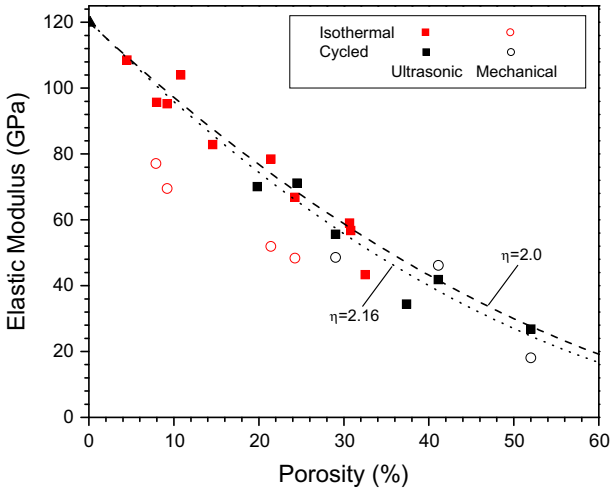

Fig. 8. Plot of Young's modulus vs. porosity with measured data as symbols and predictions from the Gibson–Ashby model (Eq. (10)) as lines.

In Fig. 8, the foam Young's moduli, determined by the ultrasonic method and by compressive testing, are plotted as a function of porosity. While both measurements show a decreasing trend with increasing porosity, the latter method provides lower values of stiffness because of microplasticity at stress concentration regions produced by pores.

4. Discussion

4.1. Modeling of foaming kinetics

4.1.1. Isothermal conditions

The relationship between foaming rate and initial porosity existing in Fig. 1 can be explained by the fact that initial porosity scales with the amount of argon gas entrapped in the alloys, and thus the driving force for the expansion. In Fig. 1b, the growth of porosity slows abruptly as the pores open to the surface of the foam, leading to the escape of the gas and the elimination of the internal pressure driving the pore growth. The subsequent decrease in porosity indicates that sintering is closing the pores after the gas has escaped. The models presented here only address the first stage of foaming, when pores have not merged with each other or the sample surface.

Murray and Dunand [24] described an analytical model for foaming based on creep expansion of a thick walled pressure vessel [39]. A single gas-filled spherical pore is taken to be a representative section of a larger multi-pore system. Depending on the sign of the isostatic stress, this model can describe either the densification rate [40,41] or the expansion, or foaming rate $\dot{f}$ as a function of the instantaneous porosity f:

$$\dot{f} = \frac{3A}{2}\frac{f(1-f)}{(1-f^{1/n})^n}\left(\frac{3}{2n}P_{eff}\right)^n \quad (3)$$

where P_{eff} is the effective gas pressure that drives foaming, discussed in more detail below. The material- and temperature-dependent constant A and the creep exponent n describe the uniaxial power-law creep equation for the bulk metal:

$$\dot{\varepsilon} = A\sigma^n \quad (4)$$

where $\dot{\varepsilon}$ is the uniaxial creep rate and σ is the uniaxial stress. The constant A can be further expressed as $A = A'\exp(-Q/RT)$, where Q is the creep activation energy, T is the temperature, R is the gas constant and A' is a material-dependent constant. These parameters for Ti–6Al–4V in the β-field have been experimentally determined as $A' = 0.72\ \text{MPa}^{-2.8}\ \text{s}^{-1}$, $Q = 153\ \text{kJ mol}^{-1}$ and $n = 2.8$ [29]. Due to the rapid drop in gas pressure as the pore expands, the material is assumed to reach secondary, power-law creep rapidly, and primary creep is neglected.

Finite-element modeling (FEM) using a commercial software (Abaqus version 6.3) was performed to model pore expansion for both axisymmetric two- and three-dimensional (2- and 3-D) unit cells, shown in Fig. 9. Both models use mirror boundary conditions to simulate an infinite field of elastically interacting pores arranged on a simple cubic lattice. Previous work [24] demonstrated that the foaming rates calculated with the axisymmetric 2-D numerical model and the pressure-vessel analytical model (Eq. (3) with the ideal gas law and no surface tension correction) matched well up to ~8% porosity, beyond which computational convergence issues prevented further calculations. The newer software version used here shows that agreement between the 2-D model, the 3-D model and the analytical model extends to ~25% porosity (Fig. 9). Due to this excellent agreement, the least computationally expensive analytical model (Eq. (3)) was chosen to compare to experimental data.

As compared to previous work [24], which assumed ideal gas behavior and negligible surface tension of the pores, we consider here, as done initially in Ref. [42], the non-ideal behavior of Ar at high-pressure and the surface

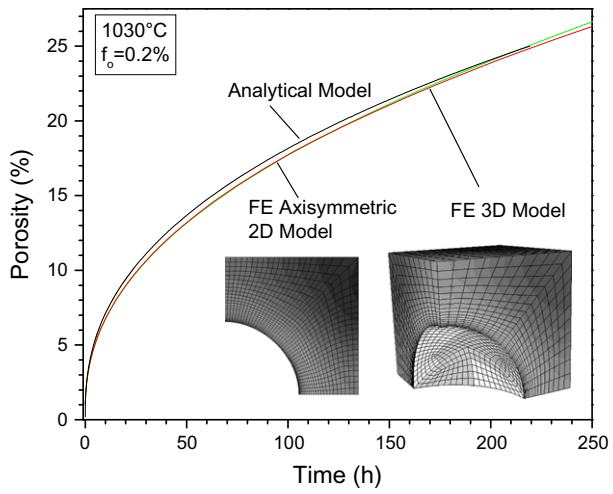

Fig. 9. Calculated foaming curves for 1030 °C isothermal anneal with an initial porosity of 0.2% showing the curve for the continuum model (Eq. (3), for ideal gas and no surface tension) and finite-element modeling (2-D and 3-D, with meshes shown in the inset).

tension of Ti–6Al–4V. The argon pressure P_{vir} is given by the Virial equation of state:

$$\frac{P_{vir}V_m}{RT} = 1 + \frac{B}{V_m} \tag{5}$$

where V_m is the Ar molar volume and B is a fitting parameter determined by a Taylor expansion as:

$$B = a_1 + a_2\left(\frac{T_o}{T} - 1\right) + a_3\left(\frac{T_o}{T} - 1\right)^2 \tag{6}$$

where, for argon, fitting parameters are $T_0 = 273$ K, $a_1 = -16$ m^3, $a_2 = -60$ m^3 and $a_3 = -10$ m^3 [33].

In the current experiments, the Virial equation leads to ~8% less gas in the pores than calculated from the ideal gas law. This difference affects significantly the initial foaming rates and the final porosity achievable in low backfill experiments. This non-linear effect also limits the use of higher HIP pressures to enhance foaming kinetics.

For small pore volumes, the surface tension becomes sizeable as compared to the gas pressure, and will tend to close the pores. In previous work done on vacuum sintering of pores free of internal gases, the surface tension closes pores with a rate determined by the initial pore radius and the local surface tension [40]. The effective inward pressure P_s from the surface tension γ is:

$$P_s = \frac{2\gamma}{r} \tag{7}$$

where γ is the solid surface energy and r is the pore radius. Then, the net gas pressure P_0 within the pores at the end of the HIP densification (with applied pressure P_{HIP}) at equilibrium is:

$$P_o = P_{HIP} + P_s \tag{8}$$

from which the initial pressure at the foaming temperature can be calculated using the Virial equation. Similarly, the effective pore pressure during foaming, P_{eff}, is reduced by the surface tension as:

$$P_{eff} = P_{Vir} - P_s \tag{9}$$

The surface energy of solids is difficult to measure experimentally [43]. Even where data on surface tension in solids has been collected, it is most often pure metals [44–46]. Due to a lack of literature data for Ti–6Al–4V, the surface tension for pure titanium at 90 °C below the melting point, $\gamma = 1.70$ N m^{-1} [44], was used here.

At the start of foaming, the effect of surface tension is minimal, as it represents in the present experiments 1–2% of the internal gas pressure. Surface tension becomes more important as the pores grow, because the pressure due to surface tension is inversely proportional to the pore radius (Eq. (7)) while the argon pressure is inversely proportional to the cube of the radius. Ultimately surface tension prevents the pores from all further growth when the internal gas pressure equilibrates with the surface tension pressure (assuming no external pressure, i.e. foaming in vacuum).

Modeling the effect of a pore size distribution is complex since the foaming rate is dependent on the pore size via Eqs. (8) and (9). Previous work has assumed a single average pore size rather than a distribution of porosity. Experimentally, the pores in the as-HIP samples B1–B4 are too small for metallographic techniques to provide accurate size distributions. The as-HIP pore distributions are then determined from a series of simulations using Eqs. (3)–(9) where, for each initial porosity, the initial pore radius is varied. These simulations show that there is a linear relationship between the initial and the final pore radius which is dependent on the internal pressure, surface tension and foaming time. Using this result, an as-HIP pore distribution, shown in Fig. 10, is calculated for each foam B1–B4 from their respective experimental Saltykov distributions shown in Fig. 6.

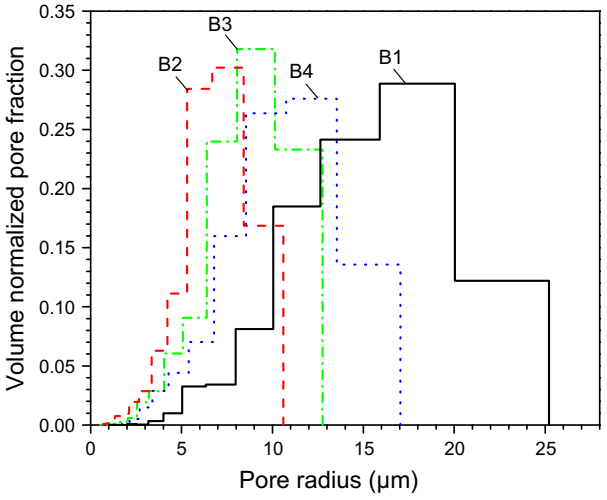

Fig. 10. Plots of volume-normalized pore fraction vs. pore radius in the as-HIP state calculated for various initial porosity.

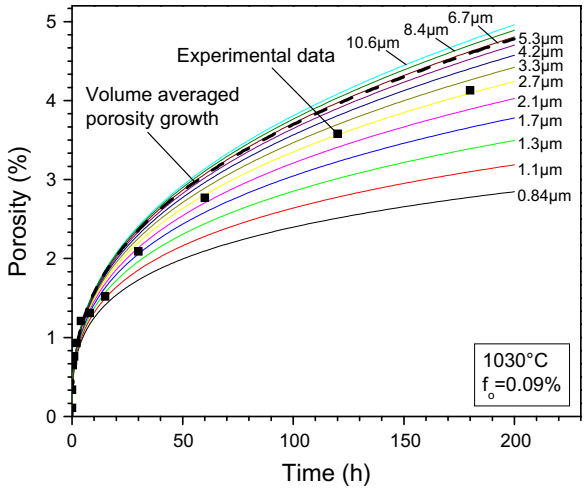

Fig. 11. Isothermal foaming curves for initial porosity of 0.09% and various pore radius, as calculated from Eqs. (3)–(9), with the bold dashed line as the volume averaged line. Experimental data for sample B2 is also shown.

The time evolution of porosity was calculated from Eqs. (3)–(9) for various initial pore radii. The overall specimen expansion was calculated by weighing the contribution of each pore radius by its initial fraction, as illustrated in Fig. 11 for sample B2. The foaming curve was then matched to the closest individual pore curve to find an effective pore radius r_0, which is 5.3 μm for the experimental foaming curve shown in Fig. 11 for sample B2 with $f_0 = 0.09\%$. These effective pore radii are determined in a similar manner as 6.4, 6.8 and 12.5 μm for samples B3 ($f_0 = 0.24\%$), B4 ($f_0 = 0.36\%$) and B1 ($f_0 = 0.48\%$), respectively.

Foaming curves calculated from Eqs. (3)–(9) with the above r_0 values are shown in Fig. 12. Given the many simplifications used in the model, satisfactory agreement with the experimental foaming curves is achieved for samples B2–B4 with the three lowest initial porosities ($f_0 = 0.09\%$, 0.24% and 0.36%). Modification to the original model [24] (Virial pressure equation and non-zero surface energy) improve agreement with the experimental curves for all but the highest initial porosity sample. For sample B1 with the highest initial porosity ($f_0 = 0.48\%$), the predicted foaming curve is significantly lower than the measured one. The most likely cause for this discrepancy is an error in the initial porosity measurement of the sample: iron from the HIP tube may have not been completely removed during sample preparation, thus increasing the sample density and decreasing the calculated initial porosity. A very small amount of iron, 2 mg, can completely account for this error: by increasing the initial porosity from 0.48% (with iron) to 0.59% (without iron), a good fit with the experimental curve is achieved.

4.1.2. Thermal cycling conditions

At low stresses, transformation superplasticity results in enhanced strain rates as compared to creep deformation [26,28–31]. This mechanism is active under multiaxial stress state [30,31], and has been shown, in CP-Ti, to enhance densification of pores subjected to external pressure [40,41], or, alternatively, enhance the expansion of internally pressurized pores [26,28–31]. In uniaxial experiments, the strain increment accumulated after each transformation is proportional to the applied stress. Thus, when cycling occurs at a constant heating and cooling rate over many cycles, the average strain rate is proportional to the applied stress, i.e. the power-law creep equation (Eq. (4)) shows a stress exponent of unity. Transformation superplasticity has been measured in uniaxial tension for dense Ti–6Al–4V, and for the same temperature range (840–1030 °C) and the same 8 min cycling period used in the present foaming experiments: the average stress exponent is $n = 1.1$, and the creep constants is $A = 2.65 \times 10^{-6}\,\mathrm{MPa}^{-1.1}\,\mathrm{s}^{-1}$. Decreasing the cycling period is

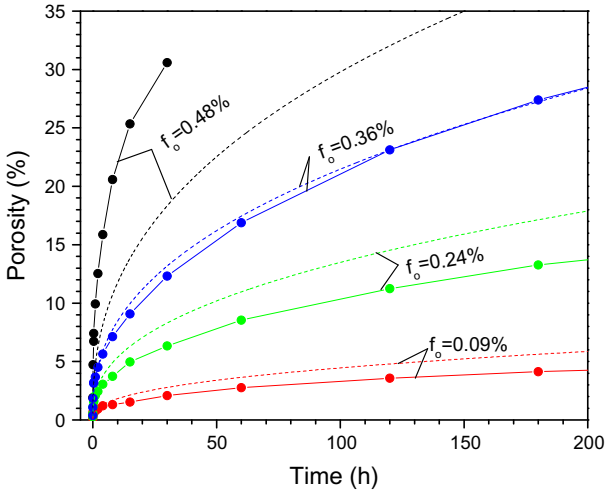

Fig. 12. Isothermal foaming curves for various initial porosities calculated from Eqs. (3)–(9), with experimental data for samples B1–B4 shown for comparison.

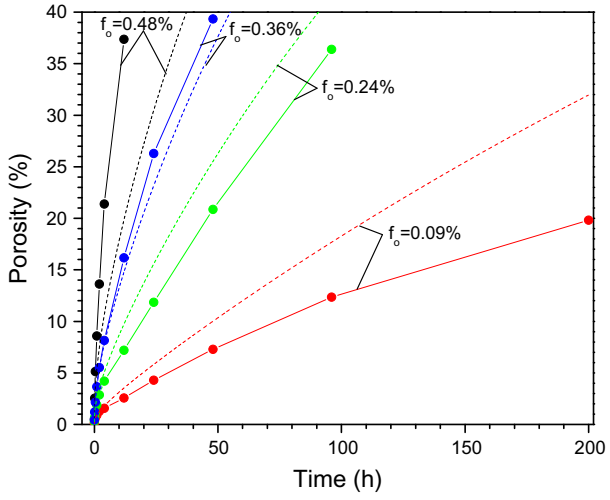

Fig. 13. Foaming curves for 840–1030 °C cycling for various initial porosities calculated from Eqs. (3)–(9), with experimental data for samples B1–B4 shown for comparison.

expected to increase the average strain rate, and thus the foaming rate. Fig. 2a, however, shows no significant improvement, as also previously reported during uniaxial deformation of Ti–6Al–4V for cycling periods of 4–10 min [30]. This effect was assigned to incomplete phase transformation due to limitations in heat transfer and transformation kinetics, reducing the internal mismatch responsible for the strain increment. Thus, faster cycling provides more transformation events, but with less strain per event, so the average strain rate remains unchanged.

Foaming curves calculated from Eqs. (3)–(9) with the same r_0 values as used in Fig. 12 are shown in Fig. 13, where the contributions of isothermal and cyclic foaming are added in Eq. (3) with the creep and superplasticity parameters for Ti–6Al–4V. The contribution to foaming from creep becomes negligible for porosities above 10%. As in the isothermal case (Fig. 12), calculation are in reasonable agreement with the experimental foaming curves for samples B2–B4 with the lowest initial porosities ($f_0 = 0.09\%$, 0.24% and 0.36%). The discrepancy for sample B1 with the highest initial porosity ($f_0 = 0.48\%$) is of the same sign and magnitude as for the isothermal case (Fig. 12), which confirms that it may be due to an initial density error, as discussed above.

4.2. Foam mechanical properties

4.2.1. Stiffness

The Gibson–Ashby model provides a simple relationship between the foam's Young's modulus E and the foam's density ρ:

$$\frac{E}{E_o} = \left(\frac{\rho}{\rho_o}\right)^{\eta} \tag{10}$$

where E_o and ρ_o are the Young's modulus and bulk density of the dense material and the exponent η is 2 in the original model [47] and allowed to fluctuate in the expansion by Wanner [48]. As shown in Fig. 8, good agreement is obtained between predictions from Eq. (10) and the ultrasonically measured foam stiffnesses, with the free parameter E_o taking a value of 120 GPa, which is within the range expected for dense, pore-free Ti–6Al–4V [49]. Wanner [48] showed that pore shape and orientation can be taken into account by allowing the exponent η to depart from its value of 2. A best-fit procedure on the ultrasonic data in Fig. 8, where both E_o and η vary, results in values of $E_o = 120$ GPa and $\eta = 2.16$, and a further slight improvement in agreement. Similarly, previous data on unalloyed titanium foams with 1–44% porosity was best fitted for $\eta = 2.16$ [19]. The Young's modulus of the foam with the highest porosity (52%) is 26.8 GPa (ultrasonic measurement) or 18.1 GPa (compressive measurement), which is close to the stiffness of cortical bone (12–17 GPa) [50]. Better matching of elastic moduli reduces stress shielding in bone-replacement implants, thus delaying implant loosening [51].

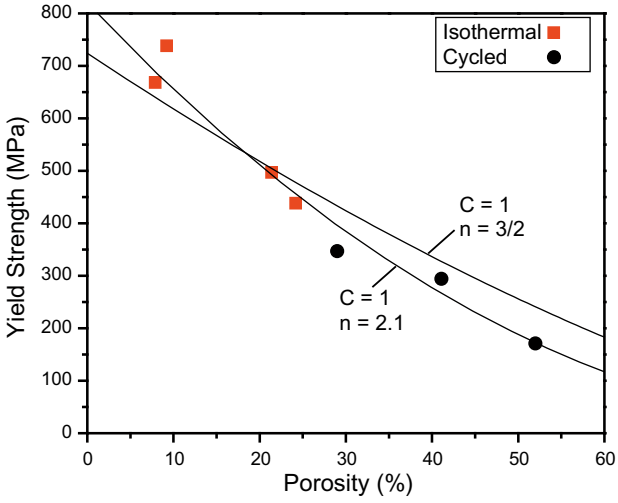

Fig. 14. Yield stress (0.2% offset) as a function of porosity with two best-fit lines from Eq. (11).

4.2.2. Compressive properties

The compression stress–strain curves are smooth and without serrations, which is typical of ductile titanium foams with equiaxed, uniform porosity [10,36]. As expected, the curves show the following trends with increasing porosity: (i) decreasing stiffness in the elastic range, where cell walls are deflecting elastically; (ii) decreasing yield stress, marking the onset of large scale plastic deformation; (iii) decreasing slope of the Plateau region, where cells collapse and plastic deformation is extensive; and (iv) increasing value of strain for onset of densification. Fig. 14 shows a plot of the 0.2% offset yield stress vs. porosity. Also plotted in this figure is the Gibson–Ashby relationship between the foam yield stress σ_y and the foam density ρ as [47]:

$$\frac{\sigma_y}{\sigma_{yo}} = C\left(\frac{\rho}{\rho_o}\right)^{3/2} \tag{11}$$

where σ_{yo} is the yield stress of the dense material and C is a fitting parameter taking values in the broad range of 0.1–2, with values greater than 0.3 expected from microcellular modeling [52]. Using a value of $C = 1$, Eq. (11) is best fitted to the experimental data for $\sigma_{yo} = 724$ MPa. If the exponent in Eq. (11) is not fixed, a best-fit calculation with $C = 1$ results in a value of 2.1 for the exponent and $\sigma_{yo} = 818$ MPa for the yield stress. Both best-fit lines are plotted in Fig. 14. As expected, these values are close to the 770–880 MPa values reported for beta-annealed Ti–6Al–4V [53].

5. Conclusions

Porous Ti–6Al–4V is created by expansion of pressurized argon trapped in micron-size pores during a prior powder-consolidation step. Pore expansion occurs by deformation of the surrounding matrix under isothermal conditions (1030 °C) or by thermal cycling (840–980 or

840–1030 °C) across the allotropic temperature range of Ti–6Al–4V. The following results are found:

- Isothermal foaming, where pores expansion is controlled by creep deformation of the surrounding matrix, is slower than foaming with temperature cycling, which activates transformation superplasticity. Superplastic foaming also delays pore wall fracture and the concomitant gas escape, thus increasing the maximum porosities achievable in the foams.
- As initial preform porosity is raised from 0.09% to 0.48% (by increasing the amount of trapped Ar by increasing the backfill pressure), initial foaming rates (time to 5% porosity) increases by a factor of 60 for cycling foaming and by a factor of >2000 for isothermal foaming due to the increase in internal pressure and the resulting increase in deviatoric stresses within the matrix. Times to achieve maximum porosity also decrease rapidly with increasing initial porosity.
- Experimental foaming curves (porosity vs. time) before the onset of gas escape are successfully modeled for both creep and superplastic conditions using a simple pressure-vessel model, modified to take into account the non-ideal behavior or Ar under high pressures, and the sintering effect of surface tension, which is dependent on pore size.
- As the foam porosity increases from 8% to 52%, the yield stress decreases from 670 to 170 MPa and the Young's modulus decreases from 120 to 28 GPa, in general agreement with the Gibson–Ashby models for foam stiffness and strength. Foams with the highest porosity are attractive for bone-replacement implants, since they exhibit a combination of high strength (needed for fatigue resistance), low stiffness (useful to reduce stress shielding) and open porosity (enabling osseo-integration).

Acknowledgments

This research was supported by the US National Science Foundation through Grant DMR-0505772. S.M.O. also acknowledges the support of the US Department of Defense in the form of a NDSEG Fellowship.

References

[1] Alvarez K, Nakajima H. Materials 2009;2:790.
[2] Bansiddhi A, Sargeant TD, Stupp SI, Dunand DC. Acta Biomater 2008;4:773.
[3] Dunand DC. Adv Eng Mater 2004;6:369.
[4] Banhart J. Prog Mater Sci 2001;46:559.
[5] Lefebvre LP, Banhart J, Dunand DC. Adv Eng Mater 2008;10:775.
[6] Taylor N, Dunand DC, Mortensen A. Acta Metall Mater 1993;41:955.
[7] Oh IH, Nomura N, Masahashi N, Hanada S. Scripta Mater 2003;49:1197.
[8] Ricceri R, Arcuri F, Matteazzi P. J Phys IV 2001;11:51.
[9] Sypeck DJ, Parrish PA, Wadley HNG. Mater Res Soc Symp Proc 1998;521:205.
[10] Erk KR, Dunand DC, Shull KA. Acta Mater 2008;56:5147.
[11] Chino Y, Dunand DC. Adv Eng Mater 2009;11:52.
[12] Kwok PJ, Oppenheimer SM, Dunand DC. Adv Eng Mater 2008;10:820.
[13] Hong TF, Guo ZX, Yang R. J Mater Sci Mater Med 2008;19:3489.
[14] Niu WJ, Bai CG, Qiu GB, Wang Q. Mater Sci Eng A 2009:506.
[15] Lopez-Heredia MA, Goyenvalle E, Aguado E, Pilet P, Leroux C, Dorget M, et al. J Biomed Mater Res 2008;85A:664.
[16] Li X, Wang CT, Zhang WG, Li YC. Mater Lett 2009;63:403.
[17] Heinl P, Rottmair A, Korner C, Singer RF. Adv Eng Mater 2007;9:360.
[18] Kearns MW, Blenkinsop PA, Barber AC, Farthing TW. Met Mater 1987;3:85.
[19] Murray NGD, Dunand DC. J Mater Res 2006;21:1175.
[20] Murray NGD, Dunand DC. Acta Mater 2004;52:2269.
[21] Greiner C, Oppenheimer SM, Dunand DC. Acta Biomater 2005;1:705.
[22] Lagoudas DC, Vandygriff EL. J Intell Mater Syst Struct 2002;13:837.
[23] Greenwood GW, Johnson RH. Proc Roy Soc London 1965;283A:403.
[24] Murray NGD, Dunand DC. Acta Mater 2004;52:2279.
[25] Murray NGD, Dunand DC. Compos Sci Technol 2003;63:2311.
[26] Schuh C, Dunand DC. Int J Plast 2001;17:317.
[27] Schuh C, Dunand DC. J Mater Res 2001;16:865.
[28] Schuh C, Dunand DC. Scripta Mater 2001;45:631.
[29] Schuh C, Dunand DC. Acta Mater 2001;49:199.
[30] Li Q, Chen EY, Bice DR, Dunand DC. Metall Mater Trans Phys Metall Mater Sci 2007;38:77.
[31] Frary M, Schuh C, Dunand DC. Metall Mater Trans 2002;33:1669.
[32] Dunand DC, Myojin S. Mater Sci Eng A 1997;230A:25.
[33] Handbook of chemistry and physics, 81st ed. Bocar Raton (FL): CRC Press; 2000/2001.
[34] Underwood EE. Quantitative stereology. Reading (MA): Addison-Wesley; 1970.
[35] Shen H, Oppenheimer SM, Dunand DC, Brinson LC. Mech Mater 2006;38:933.
[36] Davis NG, Teisen J, Schuh C, Dunand DC. J Mater Res 2001;16:1508.
[37] Davis NG, Dunand DC. In: Ghosh AS, Sanders TH, Claar D, editors. Third global symposium on materials processing and manufacturing: processing and properties of lightweight cellular metals and structures. Seattle (WA): The Minerals, Metals and Materials Society; 2002. p. 177.
[38] Davis NG. PhD thesis, Northwestern University, 2002.
[39] Finnie L, Heller WR. Creep of engineering materials. New York City: McGraw-Hill Book; 1959.
[40] Wilkinson DS, Ashby MF. Acta Metall 1975;23:1277.
[41] Wilkinson DS, Ashby MF. The development of pressure sintering maps. New York: Plenum Press; 1975.
[42] Oppenheimer SM, Dunand DC. Mater Sci Eng A 2009;523:70.
[43] Bikerman. Surface chemistry. New York: Academic Press; 1958.
[44] Jones H. Metal Sci J 1971;5(15):15.
[45] Porter DA, Easterling KE. Phase transformations in metals and alloys. Cheltenham: Nelson Thornes; 1981.
[46] Keene BJ. Int Mater Rev 1993;38(4):157.
[47] Ashby MF, Evans A, Fleck NA, Gibson LJ, Hutchinson JW, Wadley HNG. Metal foams – a design guide. Woburn (MA): Butterworth-Heinemann; 2000.
[48] Wanner A. Mater Sci Eng 1998;248A:35.
[49] Donachie Jr MJ. Titanium a technical guide. Materials Park (OH): ASM International; 2000.
[50] Gibson LJ, Ashby MF. Cellular solids. Cambridge: Cambridge University Press; 1997.
[51] Bobyn JD, Mortimer ES, Glassman AH, Engh CA, Miller JE, Brooks CE. Clin Orthop Relat Res 1992;274:79.
[52] Despois J, Mueller R, Mortensen A. Acta Mater 2006;54:4129.
[53] Boyer R, Welsch G, Collings E. Mater Prop Handbook Titanium Alloys. Materials Park (OH): ASM International; 1994.